

AD-A172 787

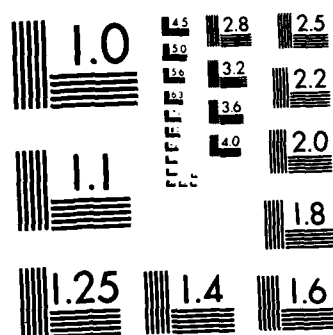
MODELING AND MEASUREMENT OF EROSION BURNING OF STICK  
PROPELLANTS(U) PENNSYLVANIA STATE UNIV UNIVERSITY PARK  
DEPT OF MECHANICAL ENGINEERING W H HSTEN ET AL 1986  
ARO-20007 4-EG DAAK29-83-K-0081 F/G 19/1

1/1

UNCLASSIFIED

NL





MICROCOPY RESOLUTION TEST CHART  
NATIONAL BUREAU OF STANDARDS 1963-A

②

UNCLASSIFIED

SECURITY CLASSIFICATION OF THIS PAGE (When Data Entered)

REPORT DOCUMENTATION PAGE		READ INSTRUCTIONS BEFORE COMPLETING FORM
1. REPORT NUMBER <b>ARO 20007.4-56</b>	2. GOVT ACCESSION NO. <b>N/A</b>	3. RECIPIENT'S CATALOG NUMBER <b>N/A</b>
4. TITLE (and Subtitle) <b>MODELING AND MEASUREMENT OF EROSION BURNING OF STICK PROPELLANTS</b>		5. TYPE OF REPORT & PERIOD COVERED <b>Reprint</b>
7. AUTHOR(s) <b>W. H. Hsieh, J. M. Char, K. C. Hsieh, and K. K. Kuo</b>		6. PERFORMING ORG. REPORT NUMBER
PERFORMING ORGANIZATION NAME AND ADDRESS <b>Department of Mechanical Engineering The Pennsylvania State University University Park, Pennsylvania 16802</b>		8. CONTRACT OR GRANT NUMBER(s) <b>DAAK 29-83-K-0081</b>
CONTROLLING OFFICE NAME AND ADDRESS <b>U. S. Army Research Office Post Office Box 12211 Research Triangle Park, NC 27709</b>		10. PROGRAM ELEMENT, PROJECT, TASK AREA & WORK UNIT NUMBERS
MONITORING AGENCY NAME & ADDRESS (if different from Controlling Office)		12. REPORT DATE
		13. NUMBER OF PAGES
		15. SECURITY CLASS. (of this report) <b>Unclassified</b>
		15a. DECLASSIFICATION/DOWNGRADING SCHEDULE
DISTRIBUTION STATEMENT (of this Report)  <b>Approved for public release; distribution unlimited.</b>		
17. DISTRIBUTION STATEMENT (of the abstract entered in Block 20, if different from Report)  <b>NA</b>		
18. SUPPLEMENTARY NOTES  <b>The view, opinions, and/or findings contained in this report are those of the author(s) and should not be construed as an official Department of the Army position, policy, or decision, unless so designated by other documentation.</b>		
19. KEY WORDS (Continue on reverse side if necessary and identify by block number) <b>Erosive Burning, k-ε Turbulent Closure, Stick Propellants, Two-Variable Joint Probability Density Function, Theoretical Modeling, Real-Time X-Ray Radiography, System Experimental Measurements,</b>		
20. ABSTRACT (Continue on reverse side if necessary and identify by block number)  <b>(see reverse side)</b>  <b>DTIC FILE COPY</b>		

**DTIC**  
**SELECTED**  
**OCT 08 1986**

AD-A172 707

UNCLASSIFIED

SECURITY CLASSIFICATION OF THIS PAGE(When Data Entered)

20.

ABSTRACT

Interior ballistic performance of unslotted-single-perforated stick propellants in a large-caliber gun could be influenced significantly by the erosive-burning effect. To analyze erosive-burning phenomena, a comprehensive model with special emphasis on the interaction of turbulence and combustion has been formulated. Experimentally, a test rig using a center-perforated cylindrical propellant grain with large web thickness (~1.0 cm) was designed, constructed, and tested. The location of the instantaneous propellant burning surface was determined by the use of real-time x-ray radiography. Based upon x-ray images, the instantaneous burning rate of NOSOL-363 stick propellant was found to be much higher (up to 3.2 times) than the strand burning rate under strong cross-flow conditions.

UNCLASSIFIED

SECURITY CLASSIFICATION OF THIS PAGE(When Data Entered)

# AIAA'86

AIAA-86-1451

## MODELING AND MEASUREMENT OF EROSIVE BURNING OF STICK PROPELLANTS

W. H. Hsieh, J. M. Char, K. C. Hsieh, and  
K. K. Kuo

The Pennsylvania State University,  
University Park, PA 16802

Accession For	
NTIS SPRI	<input checked="" type="checkbox"/>
DTIC TAB	<input type="checkbox"/>
Unannounced	<input type="checkbox"/>
Justification	
By	
Distribution/	
Availability	
Availability for	
Dist	Special
A-1	

## AIAA/ASME/SAE/ASEE 22nd Joint Propulsion Conference

June 16-18, 1986/Huntsville, Alabama

For permission to copy or republish, contact the American Institute of Aeronautics and Astronautics  
1633 Broadway, New York, NY 10019

86 10 7 1

# MODELING AND MEASUREMENT OF EROSIVE BURNING OF STICK PROPELLANTS\*

W. H. Hsieh,<sup>+</sup> J. M. Char,<sup>+</sup> K. C. Hsieh,<sup>+</sup> and K. K. Kuo<sup>+</sup>

Department of Mechanical Engineering  
The Pennsylvania State University  
University Park, Pennsylvania 16802

## Abstract

Interior ballistic performance of unslotted single-perforated stick propellants in a large-caliber gun could be influenced significantly by the erosive burning effect. To analyze erosive burning phenomena, a comprehensive model with special emphasis on the interaction of turbulence and combustion has been formulated. Experimentally, a test rig using a center-perforated cylindrical propellant grain with large web thickness (~1.0 cm) was designed, constructed, and tested. The location of the instantaneous propellant burning surface was determined by the use of real-time X-ray radiography. Based upon X-ray images, the instantaneous burning rate of NOSOL-363 stick propellant was found to be much higher (up to 3.2 times) than the strand burning rate under strong cross-flow conditions.

## Nomenclature

a	Flux model absorption coefficient, m <sup>-1</sup>
A <sub>i</sub>	preexponential factor of i <sup>th</sup> species, m <sup>3</sup> /kmol-s
b	covolume of Noble-Abel equation of state, m <sup>3</sup> /kg
C <sub>1</sub> ..C <sub>4</sub>	turbulence constants for k and ε equations
C <sub>p</sub>	constant pressure specific heat, J/kg-K
C <sub>R1</sub> , C <sub>R2</sub>	turbulence constants for transport equation of reactiveness
C <sub>s</sub>	specific heat of stick propellant, J/kg-K
C <sub>u</sub>	turbulence constants for eddy viscosity
DR1	group of species pyrolyzed from propellant surface having delayed reactions
DR2	delayed reaction species generated from O and F species
E <sub>a</sub>	activation energy, J/kmol
E <sub>b</sub>	black-body emissive power, = σT <sup>4</sup> , J/m <sup>2</sup> -s
F	fuel-rich species pyrolyzed from propellant
H	$\sum Y_i h_i + u_i u_i / 2$ , stagnation enthalpy of i <sup>th</sup> species, J/kg
I <sub>r</sub>	outward radiation flux in positive radial direction, W/m <sup>2</sup>
J <sub>r</sub>	inward radiation flux in negative radial direction, W/m <sup>2</sup>

k	turbulence kinetic energy, m <sup>2</sup> /s <sup>2</sup>
L	interaction length of X-ray and propellant sample
m	linear attenuation coefficient for photoelectric absorption
O	oxidizer species pyrolyzed from propellant surface
p	pressure, N/m <sup>2</sup>
P	final product species
q <sub>rad</sub>	radiative heat flux absorbed by the solid propellant surface, W/m <sup>2</sup>
Q <sub>s,ref</sub>	surface heat release due to pyrolysis at reference temperature, J/kg
r <sub>b</sub>	propellant burning rate, m/s
r <sub>i</sub>	inner radius of perforation, m
r <sub>o</sub>	outer radius of stick propellant, m
R	gas constant, J/kg-K
R <sub>A</sub> , R <sub>B</sub>	reactednesses defined in Eqs.(3A) and (3B)
R	selectivity
S	flux-modeling scattering coefficient, 1/m
t	time, s
T	temperature, K
u	gas velocity in axial direction, m/s
v	gas velocity in radial direction, m/s
W <sub>i</sub>	molecular weight of i <sup>th</sup> species, kg/kmol
x	axial coordinate, m
Y <sub>i</sub>	mass fraction of i <sup>th</sup> species, i could represent F, O, DR1, DR2, or P

## Greek Symbols

ε	turbulence dissipation rate, m <sup>2</sup> /s <sup>3</sup>
ε <sub>s</sub>	surface emissivity of solid propellant
λ	thermal conductivity, W/m-k
μ	dynamic viscosity of gas, N-s/m <sup>2</sup>
μ <sub>t</sub>	turbulent viscosity, N-s/m <sup>2</sup>
ν <sub>i</sub>	number of kmol of i <sup>th</sup> species
ρ	density, kg/m <sup>3</sup>
q	Stefan-Boltzmann constant, W/m <sup>2</sup> -K <sup>4</sup>
ω <sub>i</sub>	rate of production of i <sup>th</sup> species, kg/m <sup>3</sup> -s

## Subscripts

cl	centerline value
eff	effective
g	gas-phase
i	internal perforation region
p	propellant
s	surface

## Diacriticals

-	mass-weighted average quantity
---	--------------------------------

## Superscripts

~	fluctuation quantity in Favre averaging
---	---

\* This research represents a part of results obtained under contract No. DAAK29-83-K-0081, sponsored by Engineering Sciences Division, Army Research Office, Research Triangle Park, NC, under the management of Dr. David M. Mann. The authors would also like to acknowledge the encouragement and support of Dr. David Downs of ARDC-Dover and F. Robbins of BRL. The authors would also like to acknowledge Mr. M. Dervaux and Dr. C. Cuche of SNPE for the high-pressure fiberglass tube material.

<sup>+</sup> Graduate Student

<sup>+</sup> Distinguished Alumni Professor

## Introduction

The interior ballistic performance of unslotted single-perforated stick propellants in a large-caliber gun could be influenced significantly by the effect of erosive burning. In order to analyze and predict the performance of large-caliber gun systems using stick propellants, the erosive-burning characteristic of the propellants must be determined. In the past, erosive burning of various solid propellants was studied extensively under different cross-flow situations.<sup>1</sup> However, prior to this study, no suitable theoretical model was specifically developed to simulate erosive-burning processes occurring inside the stick perforation of low vulnerability ammunition (LOVA) propellants. This is due to the fact that LOVA propellants have a distended flame structure and introduce stronger interaction of combustion and turbulence.<sup>2</sup> This interaction cannot be properly modeled by previous theoretical approaches. Experimentally, instantaneous burning surface locations and erosive-burning rates along the internal perforation of propellant grain could not be determined because of the limitation of measurement techniques and hostile experimental conditions. It is apparent that a more sophisticated theoretical model and more advanced measurement technique is needed to characterize the erosive-burning processes occurring inside perforations of stick propellants. The objectives of this study are: 1) to formulate a theoretical model to describe erosive-burning phenomena, with special emphasis on turbulence-combustion interaction; 2) to demonstrate the feasibility of using real-time X-ray radiography<sup>3</sup> to measure the instantaneous burning surface locations of an axisymmetric stick propellant grain; 3) to display images obtained from erosive-burning tests showing the instantaneous web thickness of stick propellants; and 4) to discuss advantages and limitations of the real-time X-ray method for erosive burning measurements.

## Theoretical Modeling

The physical model considered in this study consists of two different regions: the gas phase and the solid phase. The gas-phase region is occupied by an axisymmetric turbulent reacting flow inside the perforation of an unslotted stick propellant (see Fig. 1). The solid phase is a NOSOL-363 propellant with an initial geometry of a thick-walled cylindrical tube with uniform inner and outer diameters. To study the erosive effect, only the internal perforation surface is allowed to burn.

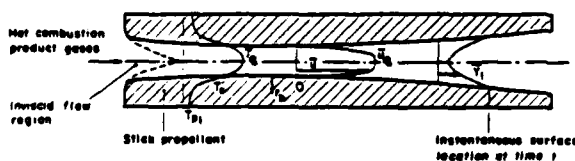


Fig. 1 Flow and temperature fields inside an unslotted single-perforated stick propellant grain

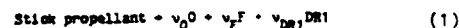
There are two basic assumptions in the formulation. First, the mean flow is treated as quasi-steady since the flow residence time is much

shorter than the characteristic times associated with conduction in the solid propellant and surface regression. This assumption has usually been adopted in past erosive-burning studies. Second, it is assumed that the heat flux in the direction normal to the propellant surface is dominant because of strong heat feedback from the flame zone. Thus, the axial heat conduction is considered to be negligible.

As pointed out by Fifer,<sup>2</sup> the combustion mechanism of nitramine-based LOVA propellants is very similar to that of nitrate ester homogeneous propellants, such as nitrocellulose/nitroglycerin (NC/NG) double-based propellants. Following the description of flame structure by Wu et al.<sup>2</sup> and Kuo et al.,<sup>3</sup> the reaction regions for gas/solid interface and gas phase consist of five different zones, i.e., preheat, foam, fizz, dark, and luminous flame zones.

Under the conditions of zero or low cross-flow velocities, Kubota<sup>6</sup> found significant flame stand-off distances for both double-base and nitramine propellants. Under strong cross-flow conditions, the flame could be highly distorted or even form pieces of flamelets; hence the location of the heat release zone produced by the reaction of pyrolyzed ingredients could be quite different from the location of pyrolysis. Finite-rate chemical reaction kinetics and the interaction of turbulence and combustion must therefore be considered in the erosive-burning model in order to simulate combustion processes inside the perforation of a stick propellant made of nitrate ester homogeneous propellants.

In modeling chemical reactions, the following reaction mechanism was adopted from Wu et al.<sup>4</sup> For surface pyrolysis of stick propellant, we have



where O represents the oxidizer-rich gases (such as NO<sub>2</sub>) pyrolyzed from the surface, F represents the fuel-rich species (such as CH<sub>2</sub>O), and the remaining species are designated as the first group of delayed reaction species, DR1. Three chemical reactions considered to take place in the gas phase are



where DR2 represents the intermediate product due to the reaction in the fizz zone. After a delay in the dark zone, the second group of delayed reaction species reacts in the luminous flame zone to generate the final product. Group 1 of delayed reaction species also forms the final product in the final flame.

The stoichiometric coefficients,  $v_i$ 's, in Eqs. (2A-2C) are determined from the mass balance

of the above three reactions. The heat of formation of these representative groups of species is obtained from the chemical equilibrium code (CEC76).<sup>7</sup> Detailed procedures are described in Refs. 4 and 5.

It is well-known that one major aspect in the modeling of turbulent reacting flow lies in the handling of the time-averaged chemical production term which is complicated by the interaction of turbulence and combustion. The effect of inevitable fluctuations of flow properties in this source term is difficult to model. One logical way to circumvent this difficulty is to adopt a two-variable joint probability density function (pdf) to obtain statistically averaged physical properties.<sup>8</sup>

The approach used in modeling the chemical production term is similar to that of Janicka and Kollmann<sup>9</sup> in their studies of turbulent H<sub>2</sub>-air diffusion flames. The present approach differs in the selection of independent variables. Janicka and Kollmann used the mixture fraction with a single reactedness; the present approach adopts two reactednesses. This is due to the fact that in premixed flames it is impossible to use mixture fraction as one of the independent variables. One specific feature of the present approach is similar to that of Bray and Moss,<sup>10</sup> who also used a joint pdf with two reactednesses as independent variables. In their studies, two consecutive reactions were used to simulate hydrocarbon-air combustion, while a set of competitive and consecutive reactions are considered in the present study.

The two independent variables chosen for the pdf are reactednesses of reactions (2A) and (2B). They are defined as

$$R_A = \frac{Y_F - Y_{F,u}}{Y_{F,b} - Y_{F,u}} \quad (3A)$$

$$R_B = \frac{Y_{DR1} - Y_{DR1,u}}{Y_{DR1,b} - Y_{DR1,u}} \quad (3B)$$

The transport equations for mean reactednesses and mean square fluctuations of reactednesses are given as

$$\bar{u} \frac{\partial \bar{R}}{\partial x} + \bar{v} \frac{\partial \bar{R}}{\partial r} = \frac{1}{r} \frac{\partial}{\partial r} \left[ r \left( \frac{\mu}{S_{c,eff}} \right) \frac{\partial \bar{R}}{\partial r} \right] + \bar{\omega}_R \quad (4)$$

$$\begin{aligned} \bar{u} \frac{\partial \overline{R^2}}{\partial x} + \bar{v} \frac{\partial \overline{R^2}}{\partial r} = & \frac{1}{r} \frac{\partial}{\partial r} \left[ r \left( \frac{\mu}{S_{c,eff}} \right) \frac{\partial \overline{R^2}}{\partial r} \right] + C_{R1} u_c \left( \frac{\partial \bar{R}}{\partial r} \right)^2 \\ & - C_{R2} \bar{\omega}_R \overline{R^2} + 2 \bar{R} \bar{\omega}_R \end{aligned} \quad (5)$$

where  $\bar{R}$  can be either  $\bar{R}_A$  or  $\bar{R}_B$ .

In general, there are two approaches in determining the relationship between the pdf and the two selected variables. One approach is to solve the equation of evolution of the pdf. The modeling of the pdf evolution equation was proposed by Dopazo,<sup>11</sup> Pope,<sup>12</sup> and O'Brien,<sup>13</sup> and

applied to turbulent diffusion flame by Janicka et al.<sup>14</sup> This approach was not adopted in the present study because of the extraordinary numerical effort required to solve the evolution equation. The second approach, to assume a functional relationship between the pdf and selected variables, has been used extensively in calculation of different turbulent diffusion or premixed flames.<sup>9,10</sup> In this study, a simple beta functional form was chosen to relate the pdf to the two reactednesses and their variants. The beta pdf<sup>15</sup> is defined as

$$\rho(R) = \frac{R^{a-1} (1-R)^{b-1}}{\int_0^1 R^{a-1} (1-R)^{b-1} dR} \quad (6)$$

where

$$a = \bar{R} \left[ \frac{\bar{R}(1-\bar{R})}{\bar{R}^2} - 1 \right] \quad (7)$$

$$b = (1-\bar{R}) \left[ \frac{\bar{R}(1-\bar{R})}{\bar{R}^2} - 1 \right] \quad (8)$$

Under the assumption that  $R_A$  and  $R_B$  are not correlated, the joint probability function,  $\rho_J(R_A, R_B)$ , can be expressed as

$$\rho_J(R_A, R_B) = \rho(R_A) \cdot \rho(R_B) \quad (9)$$

By using pdf, mean chemical production terms in Eqs. (4) and (5) can be expressed as

$$\bar{\omega}_R = \int_0^1 \int_0^1 \bar{\omega}_R \rho_J(R_A, R_B) dR_A dR_B \quad (10)$$

$$\overline{R^2 \omega_R} = \int_0^1 \int_0^1 (R - \bar{R}) \bar{\omega}_R \rho_J(R_A, R_B) dR_A dR_B \quad (11)$$

where the instantaneous chemical production term is given by

$$\bar{\omega}_R = \begin{cases} -A_F \exp(-E_{a,F}/R_u T) \rho^{2Y_F} Y_O^{1/2} / (Y_{F,b} - Y_{F,u}) & \text{FOR } R = R_A \\ -A_{DR1} \exp(-E_{a,DR1}/R_u T) \rho^{2Y_{DR1}} Y_{DR1}^{1/2} / (Y_{DR1,b} - Y_{DR1,u}) & \text{FOR } R = R_B \end{cases} \quad (12a)$$

$$\bar{\omega}_R = \begin{cases} -A_F \exp(-E_{a,F}/R_u T) \rho^{2Y_F} Y_O^{1/2} / (Y_{F,b} - Y_{F,u}) & \text{FOR } R = R_A \\ -A_{DR1} \exp(-E_{a,DR1}/R_u T) \rho^{2Y_{DR1}} Y_{DR1}^{1/2} / (Y_{DR1,b} - Y_{DR1,u}) & \text{FOR } R = R_B \end{cases} \quad (12b)$$

For premixed flames, in circumstances in which all species are assumed to have the same coefficient of diffusion transport, the carbon element mass fraction,  $Z_C$ , and the Schvab-Zeldovich variable,  $\xi$ , can be regarded as constants, that is,



$$Z_c = \Gamma(u_c)Y_j = \text{constant} \quad (13)$$

$$\xi = Y_O - \left(\frac{u_O}{u_F}\right)Y_F = \text{constant} \quad (14)$$

The sum of the mass fractions for all species is equal to one, i.e.,

$$\sum_i Y_i = 1 \quad (15)$$

The mass fractions of all five species can be solved from five algebraic equations [including Eqs.(3A), (3B), (13), (14), and (15)] after  $R_A$  and  $R_B$  are solved from Eqs.(4) and (5).

The turbulent flow inside the center perforation of the stick propellant can be described by the following set of conservation equations for mass, momentum, total enthalpy, transport equation of turbulent kinetic energy, and transport equation of turbulent dissipation rate, as well as the equation of state in the Favre-averaged form. The following equations were derived with the following assumptions: 1) Favre-averaged flow properties are quasi-steady; 2) boundary layer is axisymmetric; 3) body force and gas-phase radiation heat transfer are negligible; 4) Soret or Dufour effects are small; and 5) Fick's law of mass diffusion is valid.

$$\frac{1}{r} \frac{\partial}{\partial r} (r^2 \bar{u}) + \frac{1}{r} \frac{\partial}{\partial r} (r^2 \bar{v}) = 0 \quad (16)$$

$$\bar{u} \frac{\partial \bar{u}}{\partial r} + \bar{v} \frac{\partial \bar{u}}{\partial r} = \frac{1}{r} \frac{\partial}{\partial r} (r^2 \bar{u}_{eff} \frac{\partial \bar{u}}{\partial r}) - \frac{d\bar{p}}{dr} \quad (17)$$

$$\bar{u} \frac{\partial \bar{u}}{\partial r} + \bar{v} \frac{\partial \bar{u}}{\partial r} = \frac{1}{r} \frac{\partial}{\partial r} \left\{ r^2 \left( \frac{\bar{u}}{r} \right)_{eff} \frac{\partial \bar{u}}{\partial r} - \left\{ u_{eff} \cdot \left( \frac{\bar{u}}{r} \right)_{eff} \right\} \frac{\partial \bar{u}}{\partial r} \right\} \quad (18)$$

$$\bar{u} \frac{\partial \bar{u}}{\partial r} + \bar{v} \frac{\partial \bar{u}}{\partial r} = \frac{1}{r} \frac{\partial}{\partial r} (r^2 \bar{u} \cdot \frac{\partial \bar{u}}{\partial r}) - u_t \left( \frac{\partial \bar{u}}{\partial r} \right)^2 \quad (19)$$

$$\bar{u} \frac{\partial \bar{u}}{\partial r} + \bar{v} \frac{\partial \bar{u}}{\partial r} = \frac{1}{r} \frac{\partial}{\partial r} (r^2 \bar{u} \cdot \frac{\partial \bar{u}}{\partial r}) - c_{\mu} \bar{u} \left( \frac{\partial \bar{u}}{\partial r} \right)^2 - c_{\epsilon} \bar{u} \frac{\partial \bar{u}}{\partial r} \quad (20)$$

$$\bar{p} = \frac{\bar{u} \bar{u}}{(\frac{1}{2} - b)} \quad (21)$$

where  $m = 1$  for axisymmetric flows.

Turbulent viscosity,  $\nu_t$ , is expressed in terms of  $k$  and  $\epsilon$  as

$$\nu_t = c_{\mu} \bar{u} \frac{\partial \bar{u}}{\partial r} \quad (22)$$

In deriving the above equations, the following relationships were used.

$$\overline{u''u''} = \nu_t \frac{\partial \bar{u}}{\partial r}, \quad \overline{v''v''} = \frac{\nu_t}{c_{\epsilon}} \frac{\partial \bar{u}}{\partial r}, \quad \overline{v''u''} = \frac{\nu_t}{c_{\epsilon}} \frac{\partial \bar{u}}{\partial r} \quad (23)$$

Turbulent constants used in the above governing equations are listed in Table I.

Table I Constants used in turbulence modeling

Constant	$C_1$	$C_3$	$C_3$	$C_4$	$C_{\mu}$	$C_{R1}$	$C_{R2}$
Value	1.0	1.3	1.57	2.0	0.09	2.7	1.79

To determine the instantaneous temperature profile in the stick propellant, as well as the surface temperature distribution, a transient one-dimensional heat conduction equation is considered. This equation is given as

$$\rho_s \frac{\partial (C T)}{\partial t} = \frac{1}{r} \frac{\partial}{\partial r} (r \lambda_s \frac{\partial T}{\partial r}) + \frac{\partial}{\partial r} \left( \frac{\text{small}}{r} \frac{\partial T}{\partial r} \right) + a \left[ (I_r - E_b) + (J_r - E_b) \right] \quad (24)$$

which takes into account the subsurface radiation absorption for translucent propellants such as NOSOL-363. The determination of the source terms containing both outward and inward radiant fluxes requires solution of the flux-transport equations. Based upon a two-flux model, the two transport equations for  $I_r$  and  $J_r$  can be given as

$$\frac{d(r I_r)}{dr} = -(a+a) r I_r + a r E_b + J_r + \frac{1}{2} a r (I_r + J_r) \quad (25)$$

$$\frac{d(r J_r)}{dr} = (a+a) r J_r - a r E_b + J_r - \frac{1}{2} a r (I_r + J_r) \quad (26)$$

A set of boundary and initial conditions must be specified to complete the theoretical formulation. At the solid-gas interface, balances of mass and energy fluxes can be written as

$$\rho_s r_b Y_{i,s} = (\bar{\rho} \bar{v})_s - \left( \rho \frac{\partial Y_i}{\partial r} \right)_s \quad (27)$$

$$-\lambda_s \frac{\partial T_s}{\partial r} \Big|_s = (\bar{q}_{rad})_{net} - \lambda_s \frac{\partial T}{\partial r} \Big|_s + \rho_s r_b (C_p - C_s) (T_s - T_{s,ref}) + Q_{s,ref} \quad (28)$$

where  $Q_{s,ref}$  is defined as the net surface heat release at reference temperature,  $T_{s,ref}$ ;  $(\bar{q}_{rad})_{net}$  is the net radiation flux on the interface, and is related to  $I_r$  and  $J_r$  by the following equation.

$$(\bar{q}_{rad})_{net} = I_r \Big|_{r=r_1^-} + \epsilon_s J_r \Big|_{r=r_1^+} - \epsilon_s E_b T_{s1} \quad (29)$$

Other boundary conditions at the solid-gas interface are

$$\bar{u} = 0, \quad \bar{v} = \rho_s \tau_b / \sqrt{g}, \quad \bar{R}_A^2 = \bar{R}_B^2 = 0 \quad (30)$$

which represent non-slip condition, mass continuity, and zero fluctuation of reactednesses, respectively. The boundary conditions for the  $k$  and  $\epsilon$  equations at the near-wall region are identical to those of Arora et al.<sup>15</sup>

When the flow inside the perforation of the stick propellant is not fully developed, flow properties are considered to be either continuous or constant at the edge of the boundary layer, i.e.,

$$\bar{u} = u_g, \quad \bar{r} = r_g, \quad \frac{\partial \kappa}{\partial r} = \frac{\partial \epsilon}{\partial r} = 0 \quad (31)$$

$$\bar{R}_A = 1, \quad \bar{R}_B = 1, \quad \frac{\partial \bar{R}_A^2}{\partial r} = \frac{\partial \bar{R}_B^2}{\partial r} = 0 \quad (32)$$

When the flow is fully developed, the symmetric conditions are used at the axis, i.e.,

$$\frac{\partial \bar{u}}{\partial r} = \frac{\partial \bar{r}}{\partial r} = \frac{\partial \kappa}{\partial r} = \frac{\partial \epsilon}{\partial r} = \frac{\partial \bar{R}_A}{\partial r} = \frac{\partial \bar{R}_B}{\partial r} = \frac{\partial \bar{R}_A^2}{\partial r} = \frac{\partial \bar{R}_B^2}{\partial r} = \frac{\partial \bar{H}}{\partial r} = 0 \quad (33)$$

The initial condition for the solid-phase heat conduction equation is

$$T_p = T_{pi} \quad \text{AT} \quad t = 0 \quad (34)$$

Boundary conditions for Eq.(24) and the radiative heat-flux equation at the gas-solid interface are

$$T_{ps} = \bar{T}_g|_r = r_i \quad (35)$$

$$J_r = (1 - \epsilon_i) \sigma \bar{T}_{g,eff}^4 - \epsilon_s \sigma T_{ps}^4 \quad (36)$$

and at the outer radius are

$$T_s|_r = r_o = T_{pi} \quad (37)$$

$$J_r = (1 - \epsilon_o) \sigma T_w^4 - \epsilon_s \sigma T_{ps}^4 \quad (38)$$

The distinct features of the model presented in this paper are:

- 1) consideration of gas-phase reactions with pdf closure to account for the interaction of combustion and turbulence;
- 2) use of two reactedness parameters to simulate delayed reactions in the dark zone of homogeneous propellants; and

- 3) treatment of subsurface radiation absorption with two-flux equations.

### Experimental Approach

#### Experimental Apparatus

Parallel to the theoretical study, an experimental investigation has been carried out to observe the erosive-burning phenomena and to establish a data base for model validation. Since stick propellants used in large-caliber guns generally have cylindrical geometry with single perforation, it is advantageous to use a test sample with cylindrical geometry to attain close simulation. Under normal circumstances, phenomena occurring in a cylindrical grain cannot be observed by conventional flow visualization techniques. This is why most researchers in the past have used two-dimensional propellant slabs as test samples. Because a real-time X-ray is now available for erosive-burning measurements, a test propellant grain with cylindrical geometry can be adopted. In order to allow a relatively long test duration (a few seconds) for surface regression-rate measurement, a thick-walled cylindrical grain with web thickness in the order of 1 cm has been used. A set of NOSOL-363 propellant samples with 2.54 cm outer diameter and 0.467 cm inner diameter has been processed for erosive-burning tests.

A test rig was designed and constructed to provide two different configurations, A and B as shown in Figs. 2 and 3, respectively. The test chamber of configuration A is made of stainless steel with thermocouple ports for subsurface temperature measurements at various locations. The main body of the test chamber of configuration B is made of LEXAN materials to facilitate X-ray penetration. Configuration B is also equipped with a fast-actuating ejection mechanism using an explosive bolt to achieve interrupted burning and propellant recovery. Ignition of the propellant charge in the driving motor is accomplished by activating the electric primer via a current input. The combustion products of the propellant charge flow from the driving motor into the test section through a converging graphite nozzle. As hot gases enter the stick-propellant perforation, the test sample is heated quickly to reach a fully ignited condition. The combustion product gases generated from the propellant sample join the product gases from the driving motor and flow through the exit nozzle to the ambient. In configuration A, the propellant grain can also be recovered by replacing the exit nozzle with a bursting diaphragm assembly.

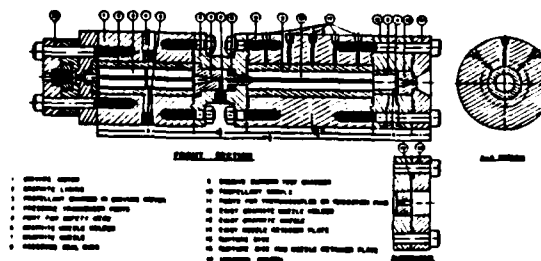


Fig. 2 Schematic diagram of test rig assembly for studying erosive-burning phenomena of stick propellants (Configuration A)

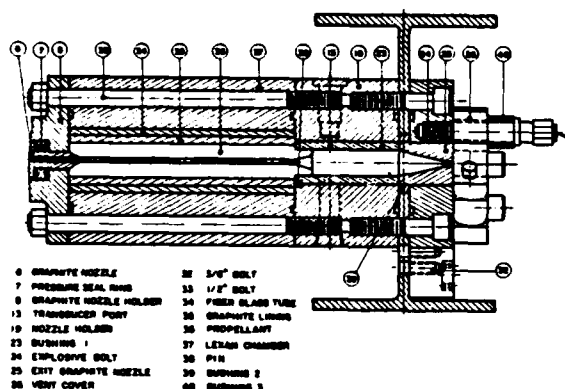


Fig. 3 Schematic diagram of test rig assembly for studying erosive-burning phenomena of stick propellants (Configuration B)

In configuration B, some physical processes occur inside the test rig. Instead of measuring subsurface temperatures, the surface regression processes are observed and recorded using real-time X-ray radiography techniques. Employing these two configurations, the erosive-burning test rig can provide the following special features:

- 1) the instantaneous inner surface location of the test sample can be observed by means of a X-ray radiography system;
- 2) the driving motor can generate high-pressure high-velocity product gases to flow over the propellant sample surface;
- 3) burning can be confined to the internal surface by using flame-retardant grease on the external surface;
- 4) ejection of the exit nozzle and propellant grain into a water tank can be achieved by incorporating an explosive bolt assembly with a timing-deady device; and
- 5) the test chamber pressure can be altered by using interchangeable exit nozzles.

#### Data Acquisition System

During the test firing with configuration B, the instantaneous burning surface location of the propellant grain is filmed by a real-time X-ray radiography system. Figure 4 shows the layout of various components in the radiography system. A continuous X-ray is generated from the Phillips MG 321 constant potential X-ray system. Two X-ray tubes [one with a focal spot combination of  $0.2 \times 0.2 \text{ mm}/3.0 \times 3.0 \text{ mm}$  (MCN 167-160 kV), the other with a focal spot combination of  $1.2 \times 1.2 \text{ mm}/4.0 \times 4.0 \text{ mm}$  (MCN 321-320 kV)] are included in the system to satisfy different penetration depth and spatial resolution requirements. A lead diaphragm is installed at the exit port of the X-ray tube head to limit the angle of divergence of the X-ray beam and to confine the beam to the measuring section of the erosive-burning test rig (this also reduces unnecessary radiation exposure to the surroundings). A second lead diaphragm with a larger opening is placed in front of the image intensifier to reduce scattered X-ray radiation and resulting noise on the fluorescent screen.

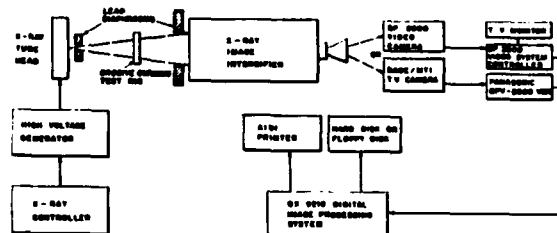


Fig. 4 Layout of real-time X-ray radiography system

After passing through the test rig, X-ray signals are transformed to fluorescent light signals on the output screen of a tri-field image intensifier (Precise Optics, Model P1 2400 ATF, 4", 6", or 9" field diameter). The input fluor of the image intensifier is made of cesium iodide with a decay time constant of 650 ns, and the output fluor is a p20 type with a 85 ns decay-time constant. These time constants are short enough to allow the motion analysis system to operate at its maximum framing rate without generating image blur.

The fluorescent light signal output from the image intensifier is recorded by a Spin Physics 2000 Motion Analysis System. This system can record up to 2000 fully digitized frames per second, or up to 12,000 digitized pictures per second with adjustable playback speed. Two cameras can be used simultaneously to film different views of the event. The motion analysis system consists of the following subsystems:

- a) a camera, with solid-state image sensor. The picture information goes to the console from the camera, and is processed into a frequency-modulated carrier that is recorded on tape.
- b) a main electronic bin, which contains the record and playback electronics, along with video output circuitry.
- c) a tape transport, which drives the half-inch tape cassette at a maximum speed of 250 inches per second.
- d) a Dage camera and Panasonic VCR, which record the event at 30 frames per second.

Digitized data is stored on a high-intensity magnetic recording tape and can be transferred to the digital image-processing system frame by frame for analysis through an IEEE-488 interface. The digital image-processing system consists of several major components:

- a) a Quantex (QX-9210) digital image processor with two pipeline point processors, each with a random access image memory of  $480 \times 640 \times 12$  bits. The processors perform real-time image enhancements, including noise reduction, image subtraction, arbitrary contrast control, roam, and zoom. The processor can also be used to conduct such high-speed image analyses as brightness histogram, local contrast stretch, area and point brightness measurements, calibrated length and area measurements, Sobel edge enhancement, and so forth;
- b) a mass storage device, consisting of both a 2.4 MB dual 8" floppy diskette drive and a 50 MB hard disk for the storage of image data; and

- c) a high-resolution videograph printer for producing large high-quality pictures on hard copies.

The advantages of using real-time X-ray radiography for erosive-burning measurements are summarized below:

- 1) No viewing window is needed to record the erosive-burning event since it is possible to observe the surface regression process occurring in a steel or optically opaque chamber.
- 2) X-ray radiography is a non-intrusive technique which will not affect the erosive-burning processes.
- 3) The technique can be applied to either 2-D or axisymmetric propellant-grain geometry.
- 4) It is a real-time data recording system. Pictures captured in the test event can be played back immediately after the test firing at a lower speed for visualization and analysis.
- 5) All data are in digital form and are convenient for recording, analysis, transfer, and storage.

#### Data Reduction

Despite the advantages listed above, the data reduction procedures for deducing the instantaneous internal diameter of a burning propellant sample is not straightforward.

Theoretically speaking, an ideal radiography image of a hollow cylindrical solid propellant with known geometry can be determined from the assumptions that 1) X-ray radiation is generated from a point source, via an infinitely small focal spot, 2) X-ray is only attenuated by photoelectric absorption, and 3) distribution of X-ray intensity over the input screen of an image intensifier is uniform. As shown in Fig. 5, the X-ray intensity distribution over the input screen of an image intensifier can be evaluated by the following equation:

$$I(\theta) = I_0 \exp[-m L(\theta)] \quad (39)$$

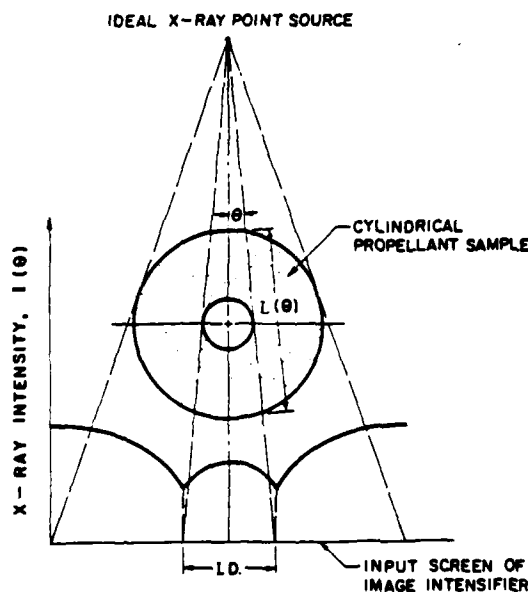


Fig. 5 X-ray intensity distribution of a hollow cylinder under idealized conditions

where  $m$  is the linear attenuation coefficient for photoelectric absorption, and  $L(\theta)$  is the interaction length of the X-ray and propellant sample. The distribution of X-ray intensity is continuous, but with two cusps at the tangent points of the internal perforation. Even though the existence of cusps is helpful in determining the inner diameter, the continuity of intensity profile makes it difficult to use direct scaling and standard-edge detection in determining the precise internal diameter of a hollow propellant sample. Two-dimensional slab samples would improve the situation since there are drastic intensity discontinuities at the edges between gas and solid propellant surfaces.

Figure 6 shows an image of a cylindrical propellant sample and an X-ray intensity profile of one scan line perpendicular to the axis obtained in an actual test firing. In this picture, the valleys of intensity are not aligned with the inner diameter due to the scale difference. Comparing Fig. 6 with Fig. 5, it is evident that the image obtained in the test firing is degraded severely and the cusps are not as distinct as those in Fig. 5. The physical mechanisms responsible for this degradation are caused by 1) the finite focal-spot size of the X-ray tube head, which generates a grainy or unclear image, 2) Compton scattering<sup>16</sup> of the test chamber and propellant sample, which becomes more dominant than photoelectric absorption when X-ray radiation energy becomes higher, 3) the nonuniform intensity distribution of X-ray radiation over the input screen of the image intensifier, and 4) the degradation caused by the image intensifier, camera, and recording system.

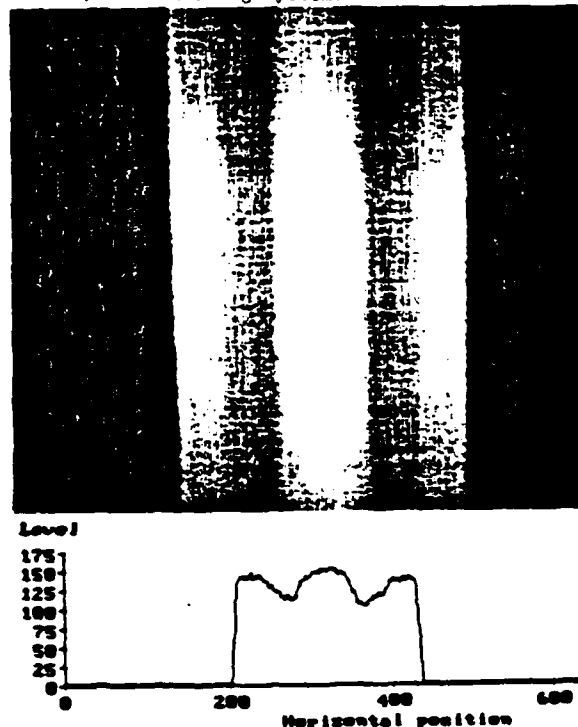


Fig. 6 X-ray image and intensity profile of a stick propellant sample

To accurately deduce the internal diameter of the propellant sample by image restoration, the degradation factors mentioned above must be properly treated. To bypass a number of the difficulties involved in image restoration, the following procedures are adopted in determining the instantaneous location of the internal burning surface of the propellant sample.

1) Generation of calibration image: A set of cylindrical propellant samples were machined to specified internal diameters for calibration purposes. The calibration images were produced by placing the machined propellant samples inside the erosive-burning test rig and exposing them to X-ray radiation at the same intensity level as test-firing conditions. The setting on the data acquisition system for calibration is also identical to that used in the actual test firing. To reduce the noise level in the calibration signal, numerous calibration images were obtained and averaged for a single specimen.

2) Comparison of images obtained in actual test firing with calibration images: The intensity distribution of the averaged calibration signals was compared with the intensity distribution of test-firing images. In comparison, a normalized cross-correlation given by

$$C_{xy} = \frac{\sum X(n)Y(n)}{\sqrt{\sum X^2(n)} \sqrt{\sum Y^2(n)}} \quad (40)$$

is used where  $X(n)$  and  $Y(n)$  are intensities of X-ray radiation of calibration image and actual test firing image, respectively.

3) Determination of internal diameter: The instantaneous internal diameter of the test propellant grain at a given location of the test propellant grain is determined from the best correlation with one of the 27 calibration propellant samples. Using this procedure, the accuracy of the diameter measurement is in the order of 0.4 mm.

#### Discussion of Results

A typical set of pressure-time traces obtained from the erosive-burning test firing is shown in Fig. 7. All gages show pressure spikes at initial time less than 0.1 s. The pressure spike is caused by the strong flow of product gases generated from the driving motor. After the initial spike, the pressures at all gage locations remain relatively constant with slight decay.

During the entire test period, the pressure at the driving motor is higher than that at the inlet nozzle or downstream cavity. This implies that the flow is unidirectional from the head end to the exit nozzle. From the magnitude of the pressure at the G3 location one can be sure that except at the end of the test firing, the exit nozzle is choked most of the time.

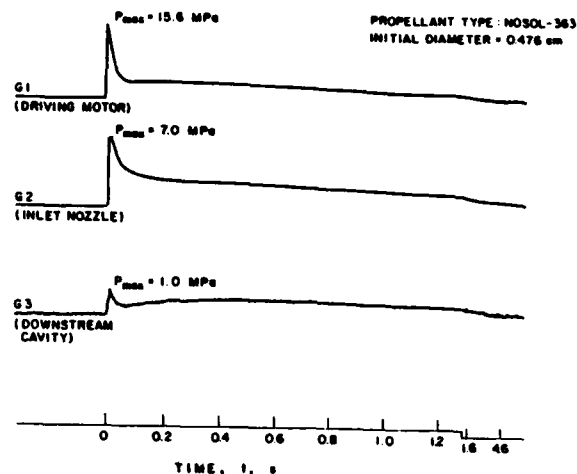


Fig. 7 A typical set of pressure-time trace (Test No. ERB-24)

X-ray images of the downstream portion of the test propellant grain were recorded on a video cassette recorder. (Due to the length limitation of the input fluor of the image intensifier, only the downstream portion is recorded.) A typical X-ray image is shown in Fig. 8. It is evident that the inner diameter of the propellant grain can be identified. The increase of internal diameter with respect to time can also be seen on the video screen.



Fig. 8 A typical X-ray image of stick propellant during test firing ERB-24

After comparison with calibration samples and carrying out data reduction procedures, the time variations of the inner diameter distributions were determined (see Fig. 9). Using the data presented in Fig. 9, the burning rates at the upstream ( $x=x_u=6.03$  cm) and downstream ( $x=x_D=15.58$  cm) locations were deduced and plotted in Fig. 10. The strand burning rate of the NOSOL-363 propellant was also calculated for evaluation of erosivity ( $r_b/r_b^0$ ) at the two locations described above. This information is plotted together with the deduced burning rate on the same figure.

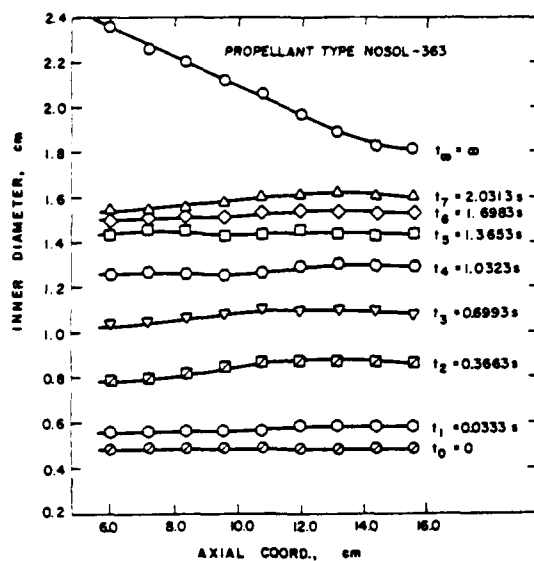


Fig. 9 Time variation of the inner diameter distribution deduced from recorded X-ray images.

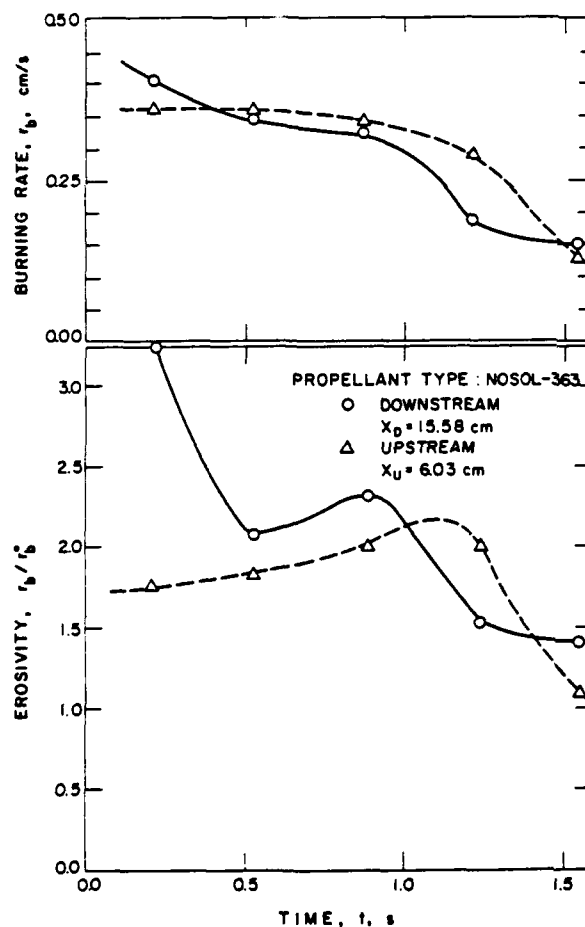


Fig. 10 Measured time variation of erosive-burning rates and erosivities at upstream and downstream locations.

Some interesting observations made from Figs. 9 and 10 are summarized below:

- 1) In the early time period ( $t < t_3$ ), the contour of the inner diameter exhibits divergence in the downstream direction due to the strong erosive burning effect exhibited there. The flow Mach number near the downstream end,  $x_D$ , is nearly sonic, and hence has very high erosivity in the order of 3.2. The Mach number near the  $x_U$  location is also quite high ( $\sim 0.6$ ), but the erosivity is about half of that at the  $x_D$  location. During this time period, the pressure gradient ( $-\partial p/\partial x$ ) decreases drastically with respect to time, and the perforation area increases rapidly. Both effects cause the erosivity at the  $x_D$  to decrease.
- 2) Between  $t_3$  and  $t_5$ , the burning rate at the upstream location catches up to and exceeds that at the  $x_D$  location. This is caused by the fact that as the perforation area opens, the flow Mach number decreases and the cross-flow effect becomes less pronounced. Due to the decrease in pressure, however, the erosivity may even exhibit a peak region before rapidly decaying. As a result of the higher burning rate at  $x_U$ , the contour of the internal perforation becomes uniform.
- 3) Between  $t_5$  and  $t_7$ , the burning rate and erosivity both decrease with respect to time at all locations. During this period, the propellant charge in the driving motor is largely consumed. Because the mass flow rate in the crossflow is produced mainly from the propellant sample, the mass flow rate in the downstream location becomes higher than that of upstream. Thus, the rate of decay of the burning rate at  $x_D$  is slower than that at  $x_U$ . As a result of this variation in burning rate, the contour of the internal perforation again becomes divergent.
- 4) The diameter distribution of the recovered propellant grain between  $x_U$  and  $x_D$  is shown in Fig. 9. This information was obtained from the X-ray image presented in Fig. 11. The contour of the port area was quite interesting. The minimum web thickness occurred at  $x = 6.05$  cm and a portion of the grain even exhibited a burn-through. The X-ray image shows a divergent section in the head end of the propellant grain; this is due to the design of the inlet graphite nozzle which protrudes into the propellant grain. Near the end of test firing, as other portions of the propellant surface are extinguished by the low pressure condition, the weak gaseous jet from the inlet nozzle can still expand and impinge on the inner surface of the propellant grain. Therefore, the burning in this portion during the extinction period produced a convergent-divergent contour.

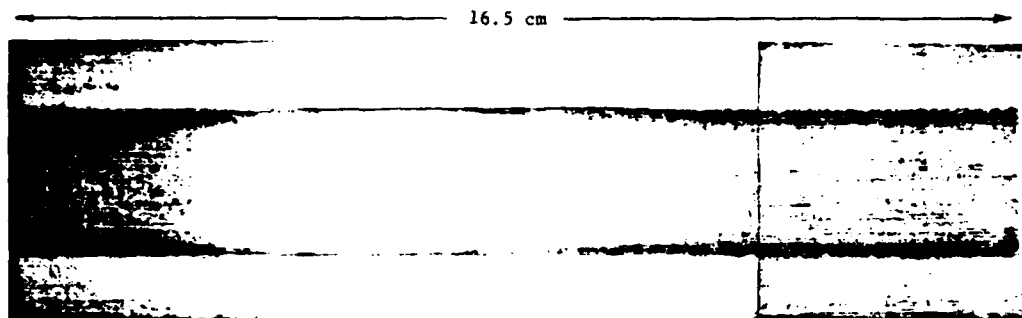


Fig. 11 X-ray image of recovered propellant grain from test firing ERB-24

#### Summary and Conclusions

- 1) A comprehensive theoretical model has been formulated to simulate erosive-burning processes of stick propellants.
- 2) The feasibility of using real-time X-ray radiography to measure the instantaneous propellant burning surface has been demonstrated.
- 3) Based upon the recorded X-ray images, the instantaneous burning rate of NOSOL-363 stick propellant has been determined under test motor operating conditions. Results show the very strong influence of cross-flow velocity on propellant burning rate. (Erosivity can be as high as 3.2.) This implies that in order to achieve accurate and realistic predictions of stick-propellant combustion performance in gun propulsion systems, the erosive-burning effect must be properly incorporated.

#### References

1. Razdan, M. K. and Kuo, K. K., Fundamentals of Solid-Propellant Combustion, edited by Kuo, K. K. and Summerfield, M., Vol. 90, Progress in Astronautics and Aeronautics, Ch. 10, 1984.
2. Fifer, R. A., Fundamentals of Solid-Propellant Combustion, edited by Kuo, K. K. and Summerfield, M., Vol. 90, Progress in Astronautics and Aeronautics, Ch. 4, 1984.
3. Bryant, L. E., Jr., "High-Speed Videography for Optical and X-Ray Imaging" Mini-Review, Los Alamos Laboratory, Sept. 1983.
4. Wu, X., Kumar, M., and Kuo, K. K., Combustion and Flame, Vol. 53, pp. 49-63, 1983.
5. Kuo, K. K., Hsieh, K.C., and Athavale, M., Proceedings of the Eighth International Symposium on Ballistics, Orlando, pp. 155-168, Oct. 1984.
6. Kubota, N., Fundamentals of Solid-Propellant Combustion, edited by Kuo, K. K. and Summerfield, M., Vol. 90, Progress in Astronautics and Aeronautics, Ch. 1, 1984.
7. Gordon, S. and McBride, B. J., NASA SP-273 Interim Revision N78-17724, March 1976.
8. Turbulent Reacting Flows, edited by Libby, P. A. and Williams, F. A., Springer-Verlag, Berlin-Heidelberg-New York, 1980.
9. Janicka, J. and Kollman, W., Seventeenth Symposium (International) on Combustion, pp. 421-430, 1979.
10. Bray, K. N. C. and Moss, J. B., Combustion and Flame, Vol. 30, pp. 125-131, 1978.
11. Dopazo, C., Acta Astronautica, 1, p. 1239, 1974.
12. Pope, S. B., Combustion and Flame, Vol. 27, pp. 299-312, 1976.
13. O'Brien, E. E., Turbulent Reacting Flows, edited by Libby, P. A. and Williams, F. A., Ch. 4, 1980.
14. Janicka, J. S., Kolba, W., and Kollmann, W., Proceeding of the 1978 Heat Transfer and Fluid Mechanics Institute, edited by Crowe, C. T. and Grosshandler, W. L., p. 296, 1978.
15. Arora, R., Kuo, K. K., and Razdan, M. K., "Near-Wall Treatment for Turbulent Boundary-Layer Computations," AIAA Journal, Vol. 20, No. 11, November 1982.
16. William, R. H., Medical Radiation Physics, Year Book Medical Publishers, Inc., Chicago, 1970.

END

11-86

DTIC